



Cite this: *RSC Adv.*, 2021, **11**, 25038

Enhanced dielectric properties with a significantly reduced loss tangent in (Mg^{2+} , Al^{3+}) co-doped $CaCu_3Ti_4O_{12}$ ceramics: DFT and experimental investigations†

Jakkree Boonlakhorn,^{ab} Jedsada Manyam,^c Sripajak Kronsuk,^{ab} Prasit Thongbai^{ab} and Pornjuk Srepusharawoot^{ab} *

$CaCu_3Ti_4O_{12}$ and $CaCu_{2.95}Mg_{0.05}Ti_{3.95}Al_{0.05}O_{12}$ ceramics were fabricated via a solid-state reaction method. A single-phase of $CaCu_3Ti_4O_{12}$ was found in these two ceramics. Very great grain size expansion was produced by co-doping with Mg^{2+} and Al^{3+} . DFT results indicate that both Mg and Al atoms preferentially occupy Cu sites, creating liquid-phase sintering decomposition at grain boundary layers. Very high dielectric permittivity of $\sim 58\ 397$ and low loss tangent of about 0.047 were achieved in a $CaCu_{2.95}Mg_{0.05}Ti_{3.95}Al_{0.05}O_{12}$ ceramic. Additionally, the temperature stability of the dielectric response was improved. Better dielectric properties in the co-doped ceramic have possible origins from enhanced grain boundary responses, especially from the influences of metastable phases and oxygen enrichment at the grain boundaries. Experimental and computational results indicate that the colossal dielectric properties in $CaCu_3Ti_4O_{12}$ ceramics might be correlated with an internal barrier layer capacitor structure.

Received 14th April 2021
 Accepted 12th July 2021

DOI: 10.1039/d1ra02896k
rsc.li/rsc-advances

Introduction

Nowadays, simple and complex oxides with their unique physical properties can be converted to essential electronic manufacturing elements to produce a variety of electronic devices.^{1–19} The development of complex perovskites for use in materials for energy storage applications has been extensively reported over the past ten years.^{1–12,20} One of the many improvements of ceramic dielectrics and related materials is used as the capacitive components of capacitors. However, almost all ceramic capacitors are produced using ferroelectric materials such as $PbTiO_3$.¹ Up to the present time, many types of advanced ceramics, ceramic–polymer composites, metal–polymer composites, and other related materials, have been candidates for capacitive materials. Considering capacitors and other electronic applications, the dielectric and electrical properties of co-doped TiO_2 ,^{13–17} co-doped SnO_2 ,^{18,19} and single- as well as co-doped $CaCu_3Ti_4O_{12}$ (CCTO)^{2–6} have been investigated and

reported. Simultaneously, ceramic–polymer and metal–ceramic–polymer composite materials have also been suggested to be new high-performance dielectric materials with outstanding physical properties, such as being flexible and environmentally friendly, among others.^{21–24} The CCTO ceramic has impressive dielectric properties in terms of its high-dielectric permittivity ($\epsilon' \sim 10^3$ to 10^5) at 1 kHz and room temperature (RT).^{2–8} The origin of the giant dielectric properties of CCTO is still unclear. An internal barrier layer capacitor (IBLC) model has been widely accepted as the primary origin of the giant dielectric response.^{2–8} Insulating grain boundaries (GB) and semiconducting grains in the CCTO structure are closely related to this dielectric model.²⁵ In addition to the microscopic scale based on an IBLC, the nanoscale barrier layer capacitance (NBLC) mechanism and the influence of domain boundaries, attributed to the potential barriers formed by the intrinsic structural defects, have also been accepted to be the nanoscopic origins of its giant dielectric response.^{26,27} In specific cases, sample–electrode contact,⁹ intrinsic defects due to charge compensation,²⁸ and other defect clusters^{29,30} are much more dominant than the IBLC, NBLC, and domain boundary effects. Therefore, the IBLC model and other possible origins should be considered to accurately describe the giant dielectric behaviour of CCTO ceramics.

There are many ways to improve the dielectric properties of CCTO ceramics by significantly reducing their loss tangent ($\tan \delta$).^{2–8} This is effective since a relatively high $\tan \delta$ is the most severe barrier of this perovskite oxide to practical use in

^aGiant Dielectric and Computational Design Research Group (GD-CDR), Department of Physics, Faculty of Science, Khon Kaen University, Khon Kaen 40002, Thailand. E-mail: spornj@kku.ac.th

^bInstitute of Nanomaterials Research and Innovation for Energy (IN-RIE), NANOTEC-KKU RNN on Nanomaterials Research and Innovation for Energy, Khon Kaen University, Khon Kaen 40002, Thailand

^cNational Nanotechnology Center (NANOTEC), National Science and Technology Development Agency (NSTDA), Pathum Thani 12120, Thailand

† Electronic supplementary information (ESI) available. See DOI: [10.1039/d1ra02896k](https://doi.org/10.1039/d1ra02896k)



capacitor applications. Preparation and sintering methods have been modified to prepare low energy loss materials.^{2,3,7,8} Also, the substitution of metal ions into the lattice has been examined to produce highly capacitive ceramics with low loss factors.³⁻⁶ According to earlier works with co-doped TiO_2 and co-doped SnO_2 , co-substitutions of $(\text{Nb}^{5+}, \text{In}^{3+})$,¹⁴ $(\text{Nb}^{5+}, \text{Al}^{3+})$,^{13,19} $(\text{Nb}^{5+}, \text{Cr}^{3+})$,¹⁸ $(\text{Nb}^{5+}, \text{Zn}^{2+})$,¹⁵ $(\text{Ta}^{5+}, \text{Al}^{3+})$,¹⁶ and $(\text{Nb}^{5+}, \text{Gd}^{3+})$,¹⁷ among others, can enhance ϵ' values while reducing $\tan \delta$. Additionally, enhancement of dielectric properties with reduced $\tan \delta$ values can be done *via* co-substitution of $(\text{Ni}^{2+}, \text{Ge}^{4+})$,^{10,11} $(\text{Sr}^{2+}, \text{Ge}^{4+})$,¹² $(\text{Zn}^{2+}, \text{Zr}^{4+})$,⁵ and $(\text{Zn}^{2+}, \text{Al}^{3+})$ ⁴ in a CCTO lattice. Interestingly, experimental results indicate that co-doping of metal ions in the CCTO structure can improve its giant dielectric response. Interestingly, previous research studies have investigated the construction and design of defects generated in the lattice of oxides to study the impact of intrinsic defects on the physical properties of each work.^{11,12,31-33} Also, earlier works with $(\text{Ni}^{2+}, \text{Ge}^{4+})$ ¹¹ and $(\text{Sr}^{2+}, \text{Ge}^{4+})$ ¹² dopants in CCTO ceramics investigated the dielectric and electrical responses as well as their origins by employing experimental and computational methods. It was found that one of two dopants could occupy some sites in unexpected ways (*e.g.*, Ge^{4+} preferentially occupies Cu^{2+} sites rather than Ti^{4+}), causing a decomposition of metastable insulating phases at GBs. Additionally, the computational results indicate that an influence of co-substitution is a decrease in oxygen loss. As a result, the total energy loss factor can be reduced in these two ways. Although investigations of co-doped CCTO ceramics have been extensively reported, only experimental factors have been presented. It is reasonable to propose that experimental work combined with computational methods based on advanced dielectric and electrical properties may provide great insights. Using the co-doping concept of our previous work, we changed dopants as $\text{Ni}^{2+} \rightarrow \text{Mg}^{2+}$ and $\text{Ge}^{4+} \rightarrow \text{Al}^{3+}$ since these conditions have not yet been reported. Thus, these preparations and characterizations were systematically made.

In this research, a solid-state reaction (SSR) method was chosen to synthesize the $\text{CaCu}_3\text{Ti}_4\text{O}_{12}$ and $\text{CaCu}_{2.95}\text{Mg}_{0.05}\text{Ti}_{3.95}\text{Al}_{0.05}\text{O}_{12}$ ceramics. Structural, dielectric, and electrical factors were systematically examined. Also, the stable structure of Mg and Al codoped CCTO structure was inspected through density functional theory (DFT). The stable location of oxygen vacancies in $(\text{Mg}^{2+}, \text{Al}^{3+})$ doped CCTO lattice was scrutinized. Details of fabrication, characterization, results, and a discussion are presented in the following.

Experimental details

1. Ceramic preparation

MgO (Sigma-Aldrich, 99.99% purity), Al_2O_3 (Sigma-Aldrich, 99.99% purity), TiO_2 (Sigma-Aldrich, 99.9% purity), CuO (Sigma-Aldrich, 99.0% purity), CaCO_3 (Sigma-Aldrich, 99.0% purity), and $\text{C}_2\text{H}_5\text{OH}$ (RCI Labscan, 99.5% purity) were used in the preparation of $\text{CaCu}_3\text{Ti}_4\text{O}_{12}$ and $\text{CaCu}_{2.95}\text{Mg}_{0.05}\text{Ti}_{3.95}\text{Al}_{0.05}\text{O}_{12}$ ceramics *via* a SSR method. First, stoichiometric quantities of starting raw metallic materials for these two conditions were mixed with $\text{C}_2\text{H}_5\text{OH}$ and zirconia balls in plastic bottles. Then,

the bottles were used as ball mills rotating at 200 rpm for 24 h. Second, the mixed raw materials were dried in an oven at 80 °C for ~24 h. Third, the resulting powders were calcined at 850 °C for 12 h. Details of forming pellet-shaped bodies have been previously published.³⁴ The pellet bodies were sintered in air at 1050 °C for 3 h. In this work, the sintered $\text{CaCu}_3\text{Ti}_4\text{O}_{12}$ and $\text{CaCu}_{2.95}\text{Mg}_{0.05}\text{Ti}_{3.95}\text{Al}_{0.05}\text{O}_{12}$ ceramics are references as the CCTO and Mg05Al05 samples, respectively.

2. Characterizations

Crystal structure and phase arrangements of the sintered samples were characterized using X-ray diffractometry (XRD, PANalytical, EMPYREAN) coupled with HighScore Plus Software Version 3.0e. The XRD patterns were collected over the 2θ range of 20°–80° using a step increase of 0.01°. The XRD data were analyzed using the Rietveld refinement method. The refinement factors are given in previous work.³⁴ A desktop scanning electron microscope (MiniSEM, SNE-4500M) was performed to investigate a morphology of our fabricated ceramics. An energy-dispersive X-ray spectroscopy (EDS) technique was used to research the dispersion of various common elements. Valence states of the Cu and Ti were determined using X-ray photoelectron spectroscopy (XPS, AXIS Ultra DLD).

3. Computational calculations

DFT calculations were done using the Vienna *Ab initio* Simulation Package (VASP)³⁵ to determine the lowest-energy configuration of the Mg and Al dopants in the CCTO structure. Moreover, the most stable position of oxygen vacancy (V_O) in the Mg and Al codoped CCTO lattice was also considered. Computational details are given in our previous work.¹² With the Projector Augmented Waves (PAW) pseudopotential used in the present work, we chose 2p and 3s valence states for Mg and 3s and 3p valence states for Al.

4. Dielectric and electrical tests

Sample surfaces were polished to prepare smooth surface layers before applying an Au film coating. A Polaron SC500 sputter coating unit was used in the Au deposition process for dielectric and electrical tests. Dielectric and electrical measurements were carried over respective temperature and frequency ranges of –60 to 210 °C and 40 to 10^7 Hz using an impedance analyzer (KEYSIGHT E4990A) coupled with a temperature controller (Delta Design Chamber 9023 model). The oscillation voltage (V_{rms}) for dielectric measurements was 500 mV.

Results and discussion

XRD patterns of the CCTO and Mg05Al05 samples are shown in Fig. 1(a). A single CCTO phase (JCPDS No. 75-2188) was found in these two ceramics. XRD spectra specify a body-centered cubic (bcc) structure with an $Im\bar{3}$ space group.³⁶ No possible impurities, such as TiO_2 , CuO , CaTiO_3 , Al_2O_3 , MgO , and other related phases, were detected. The Rietveld method was performed to analyse XRD data. Structural factors are summarized in Table 1. The R -factors, including the weighted profile R -factor (R_{wt}), the



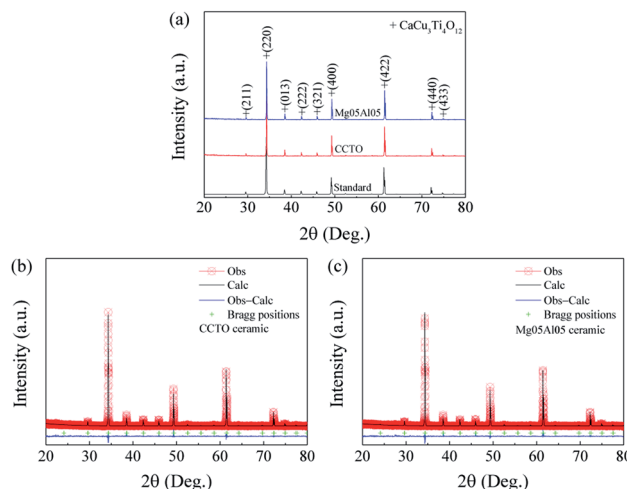


Fig. 1 (a) XRD patterns of the CCTO and Mg05Al05 ceramics. (b and c) Rietveld profile fits of CCTO and Mg05Al05 ceramics, respectively.

Table 1 Structural factors, theoretical density (ρ_T), and mean grain size (G) of the CCTO and Mg05Al05 ceramics

| Sample | CCTO | Mg05Al05 |
|--------------------------------|----------------------------|--------------------|
| a (Å) | 7.3936(0) | 7.3910(0) |
| R_{exp} (%) | 4.7389 | 4.7512 |
| R_p (%) | 4.2834 | 4.4287 |
| R_{wt} (%) | 5.6732 | 5.8849 |
| GOF | 1.4332 | 1.5341 |
| ρ_T (g cm ⁻³) | 5.0469 | 5.1174 |
| G (μm) | 2.13 ± 0.38 | 302.64 ± 78.14 |
| | 80.78 ± 37.25 ^a | |

^a Abnormal grain growth.

expected R -factor (R_{exp}), and the profile R -factor (R_p), were less than 6%. As a result of these small R -factors, the goodness of fit (GOF) factor was also relatively low (GOF \sim 1.4–1.6). Structural factors of this magnitude are acceptable values for the Rietveld refinement.³⁷ The lattice parameter (a) values of the CCTO and Mg05Al05 ceramics were 7.3936(0) and 7.3910(0) Å, respectively. Interestingly, the a value decreases when substituting with both Mg^{2+} and Al^{3+} . As reported by Sun *et al.*,³⁸ lattice parameter of $\text{CaCu}_{3-x}\text{Mg}_x\text{Ti}_4\text{O}_{12}$ ceramic with $x = 0.05$ is unchanged compared to $\text{CaCu}_3\text{Ti}_4\text{O}_{12}$. Simultaneously, the same result can be seen in the work of Nautiyal *et al.*³⁹ It is reasonable to suggest that influence of Mg^{2+} dopant does not affect to the change of lattice parameter of Mg05Al05. Interestingly, as reported by Choi and Hong,⁴⁰ the lattice parameter of $\text{CaCu}_3\text{Ti}_{3.90}\text{Al}_{0.10}\text{O}_{12}$ (\sim 7.3906 Å) is smaller than that of $\text{CaCu}_3\text{Ti}_4\text{O}_{12}$ (\sim 7.3937 Å), which is agreed with our work. Therefore, a slightly decrease in the lattice parameter of the Mg05Al05 ceramic might be originated by the Al^{3+} dopants.

To consider the locations of dopants in the CCTO host, the ionic radii and coordination numbers are used. The ionic radius of Mg^{2+} with 4 nearest neighbours is equal to that of Cu^{2+} , namely 0.57 Å.⁴¹ Although, the ionic radius of Ca^{2+} with 6

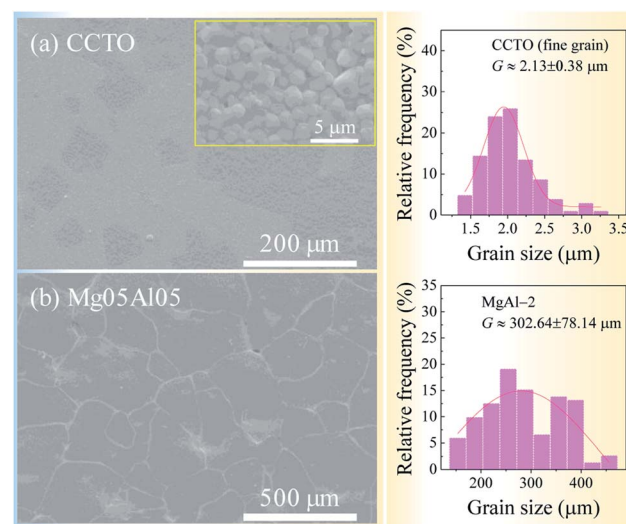


Fig. 2 SEM images and size distributions of (a) CCTO and (b) Mg05Al05 ceramics.

nearest neighbours (1.0 Å) is larger than that of Mg^{2+} . Hence, Mg^{2+} dopant might substitute at Cu^{2+} site. Al^{3+} with 4 and 6 nearest neighbours has ionic radius of 0.39 and 0.535 Å, respectively. The ionic radius of Ti^{4+} with 6 nearest neighbours is 0.605 Å which is rather close to the radius of Al^{3+} with 6 nearest neighbours. Consequently, Al^{3+} might replace at either Cu^{2+} or Ti^{4+} site. This leads us to perform the DFT calculations using the VASP code to determine the most stable positions of both Mg and Al in the CCTO lattice. Our computational investigations (see Fig. 4 and 4S in the ESI†) revealed that both Mg and Al dopants are likely to be at Cu site. The presence of Mg^{2+} and Al^{3+} at Cu sites might suppress the oxygen loss during the sintering process; thus, the dielectric and electrical properties of CCTO might be improved.

The theoretical densities (ρ_T) calculated using XRD data of CCTO and Mg05Al05 ceramics were 5.0469 and 5.1174 g cm⁻³, as listed in Table 1. Surface morphologies and grain size distributions of sintered the CCTO and Mg05Al05 samples are shown in Fig. 2. A small degree of abnormal grain growth (grain

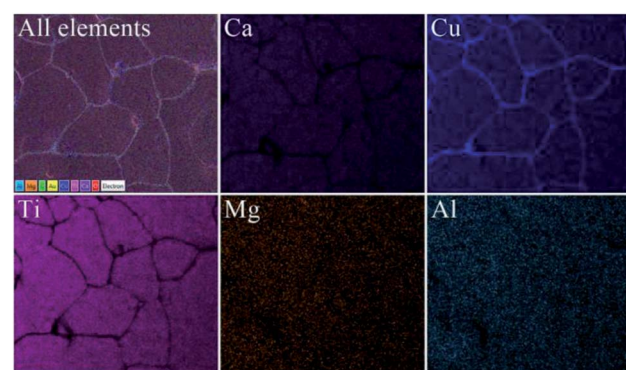


Fig. 3 EDS mapping of the Mg05Al05 ceramic showing the dispersions of Ca, Cu, Ti, Mg, and Al ions.

size $\sim 80.78 \pm 37.25 \mu\text{m}$) was surrounded by fine grains (grain size $\sim 2.13 \pm 0.38 \mu\text{m}$) in the CCTO ceramic.

Interestingly, the grains of the Mg05Al05 ceramic were primarily expanded by co-doping with Mg²⁺ and Al³⁺. The mean grain size of the Mg05Al05 ceramic was $302.64 \pm 78.14 \mu\text{m}$. The large increase in this ceramic grain size is likely associated with a liquid-phase sintering (LPS) mechanism.^{11,12,20} As disclosed in Fig. 3, EDS mapping of the Mg05Al05 ceramic showed that Mg and Al elements have suitable dispersions. Simultaneously, Ca and Ti at the grain area showed a homogeneous distribution, while these two elements are scarcely observed in the GB region. Interestingly, the Cu-rich phases were present in good quantities in the GB layers. This EDS mapping result is similar to those of other reports of the LPS mechanism.^{11,12,20}

As reported in previous research, the microstructure of Mg²⁺ doped CCTO ceramics fabricated using the SSR method and sintered at 1100°C had no significant size difference.²⁸ Thus, the Mg²⁺ dopant might not substantially impact grain size expansion at a relatively low sintering temperature of 1050°C . According to our previous work, the replacement of dopant at unexpected sites might be a significant cause of these microstructural changes.^{11,12}

It is well known that the LPS mechanism coming from the excess Cu in the CCTO host originates from the substitution of either Al or Mg at Cu sites. Consequently, the grain size is enlarged. Oppositely, this mechanism cannot be existed for the case of Al or Mg replaced at Ti sites. In general, the eutectic phases of MgO-TiO₂, MgO-Al₂O₃, CaO-TiO₂, and Al₂O₃-TiO₂ cannot be created at a temperature lower than 1200°C ,⁴² whereas, this phase is formed at 950°C in air for CuO-TiO₂. In this work, the liquid phase may be formed at lower temperature (about 850°C which is calcination temperature). This is due to the replacement of Al into Cu sites of the CCTO lattice leading to excess Cu content in the Mg05Al05. In the sintering step, the liquid phase existed at the contact zones between particles or grains in the microstructure. These can increase the diffusion rate of ions across the GB, resulting in an enhanced grain growth rate. As a result, the grain size was expressively enlarged.

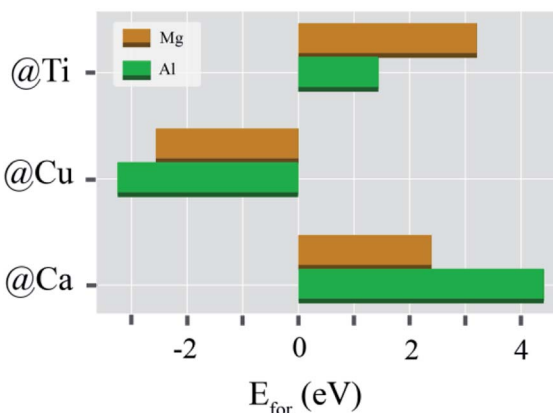


Fig. 4 Formation energies of Mg and Al occupied at Ca, Cu and Ti sites of the CCTO structure.

In the current work, to solve this assumption, DFT calculations were performed to address this issue.

In our first-principles studies, we initially tested the most preferable substitution site of both Al and Mg dopants in the CCTO host. In the current study, the CCTO structure is the $\text{Ca}_{20}\text{Cu}_{60}\text{Ti}_{80}\text{O}_{240}$ formula unit. This led us to calculate the formation energy when either Ca, Cu, and Ti sites in the CCTO lattice were replaced by Mg or Al atoms. A lower formation energy corresponds to a more stable structure.

As clearly illustrated in Fig. 4, the formation energies of Mg when Ca, Cu, and Ti atoms were replaced by Mg atoms are +2.39, -2.56, and +3.20 eV, respectively. Also, the formation energies of Al substituted at Ca, Cu, and Ti sites are +4.41, -3.25, and +1.44 eV, respectively. These results indicated that both Mg and Al are preferentially substituted at Cu sites in the CCTO host. In addition, we also performed extra calculations to calculate the formation energies when both Mg and Al dopants are in the CCTO host simultaneously. As presented by Fig. 4S in the ESI,† our calculation results revealed that Mg and Al atoms are likely to be occupied at Cu sites simultaneously. This finding is in excellent agreement with our experimental results, *i.e.*, XRD and EDS mapping. The largely increased grain sizes observed in our experiments arise from the liquid-phase sintering mechanism. This mechanism is associated with Mg and Al occupancy at Cu sites in the CCTO lattice. Generally, a eutectic liquid of CuO-TiO₂ can be created in air at 950°C .⁴³ Therefore, excess Cu generated by dopants can induce much more interaction between CuO-TiO₂ at this temperature, causing greatly increased grain sizes in the Mg05Al05 ceramic. In the Mg05Al05 sample, Mg and Al atoms are substituted into

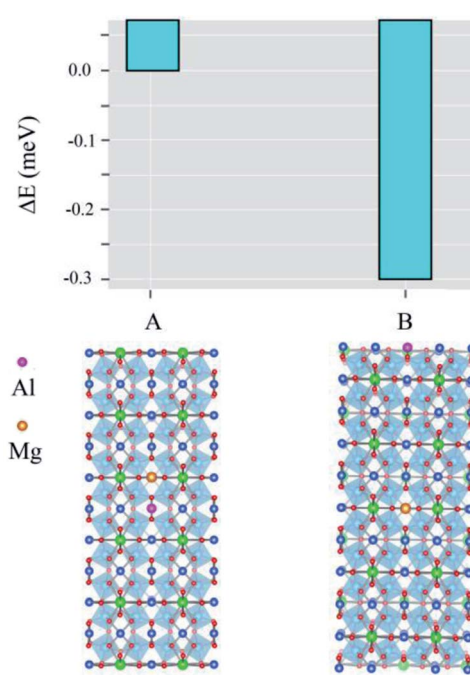


Fig. 5 Total energies when Mg and Al atoms are in close proximity (Structure A) and Mg does not interact with Al in the CCTO lattice (Structure B).



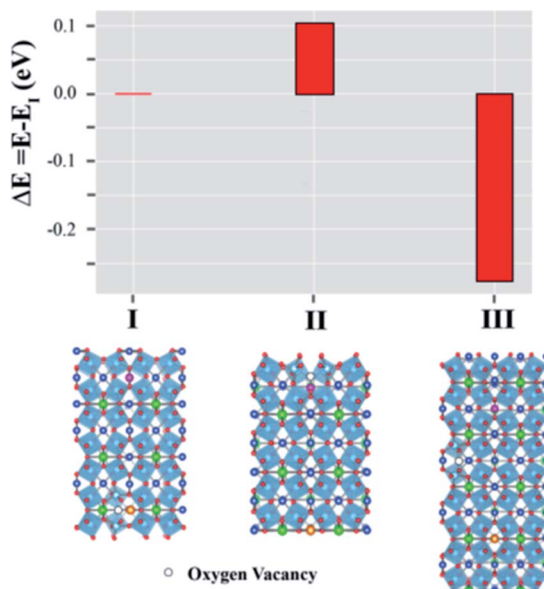


Fig. 6 Total energies of three different positions of an oxygen vacancy in the Mg and Al codoped CCTO. Structures I and II represent cases where the oxygen vacancy is close to an Mg atom, and the oxygen vacancy is close to an Al atom in the Mg05Al05 structure, respectively. Structure III indicated a case where the V_O remains independent of both Al and Mg atoms in this structure.

Cu sites in the CCTO host. Next, the most stable structure of CCTO codoped by the Mg and Al dopants needs to be determined. In the current study, we considered two different structures, namely Structures A and B.

In Structure A, depicted in Fig. 5, a Mg atom is near an Al atom in the CCTO structure. Additionally, the Mg atom does not interact with the Al atom in the CCTO host, which is presented as Structure B in Fig. 5. Our total energy calculations revealed that Structure B has a lower total energy than Structure A, 0.3 eV. Hence, Structure B is found to be the most stable. Therefore, Mg and Al atoms might homogeneously disperse in the Cu sites of the CCTO lattice.

In the present work, we also evaluated the optical property related to the energy band theory such as total density of states (DOS) of CCTO and the Mg^{2+} and Al^{3+} co-doping CCTO. These results were found in Fig. 3S of the ESI.† It was found from our calculations that the DOS of both structures is almost identical. Therefore, the optical property of the CCTO and Mg05Al05 is indifferent. Usually, oxygen vacancies (V_O) are found in our samples during the preparation process. To gain insight into the most preferable position of the V_O in the Mg05Al05 structure, the total energies of various positions of V_O in the Mg and Al doped CCTO structure were calculated. In the current work, three possible positions of V_O in the Mg05Al05 structure were inspected. Structure I of Fig. 6 represents the V_O and Mg atoms in close proximity. Additionally, the V_O interacts with the Al atom, as illustrated in Structure II of Fig. 6. The V_O is distant from both the Al and Mg atoms, as shown in Structure III in Fig. 6. Our results reveal that the structure giving the lowest total energy is Structure III. Hence, based on our calculations,

the V_O is preferentially isolated from both the Mg and Al dopant atoms. According to our stable form presented as Structure II in Fig. 6, electron-pair defects, *e.g.*, diamond or triangular shapes, are not observed. Hence, the effect of grain boundaries directly relates to the colossal dielectric properties of the Mg05Al05 structure. In other words, the giant dielectric properties of the Mg05Al05 support the internal barrier layer capacitance (IBLC) model.

According to the computational results presented in Fig. 4 and 5, the LPS mechanism observed in the Mg05Al05 ceramic might be formed by placing Al^{3+} ions into Cu^{2+} sites. A previous report showed that the LPS mechanism and oxygen enrichment at GBs could improve the dielectric properties of CCTO ceramics by enhancing the GB response.^{10–12} Hence, in this work, the resistances of grains (R_g) and GBs (R_{gb}) should increase with a reduction in the low-frequency $\tan \delta$ values. To confirm this assumption, electrical and dielectric property studies were done.

The electrical response of sintered samples was studied using an impedance spectroscopy technique. The complex impedance ($Z^* = Z' - jZ''$) can be calculated using the following relationship:

$$Z^* = Z' - jZ'' = \frac{1}{i\omega C_0(\epsilon' - i\epsilon'')}, \quad (1)$$

where $\epsilon^* = \epsilon' - j\epsilon''$ is complex dielectric constant comprised of a dielectric constant (ϵ') and total loss factor (ϵ''). $\omega = 2\pi f$ is the angular frequency, and $C_0 = \epsilon_0 A/d$ is the capacitance of free space. The Z^* plots were modelled by an ideal equivalent circuit of two parallel RC elements to analyse the impedance data. The first RC element for the grain and the second element for the grain boundary response are connected in series [the inset (3) of Fig. 7]. Z^* plots at 30 °C are given in Fig. 7 and its inset (1). At 30 °C, even though R_{gb} cannot be estimated, we can examine this factor by considering the Z^* plot's slope. R_g can estimate from a nonzero intercept at high-frequency. It was found that both CCTO and Mg05Al05 ceramics have two different electrical

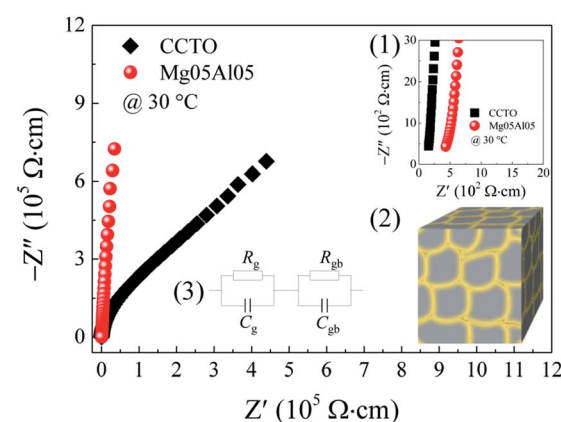


Fig. 7 Impedance complex Z^* plots at 30 °C of CCTO and Mg05Al05 ceramics. Insets (1), (2) and (3) show high-frequency Z^* plots, modelled IBLC structure, and equivalent circuit represented the electrical heterogeneous microstructure of semiconducting grain and insulating grain boundary, respectively.



components. The first indicates a tremendous resistance due to the GB responses (R_{gb}). The other specifies a small resistive component showing the R_g . CCTO structure consists of semiconducting grain and insulating grain boundary. During heating, intergranular oxygens of CCTO are released from the lattice and then V_O are formed. Some V_O sites, especially at GB layers, were filled by O^{2-} during the cooling process. However, V_O inside the grains was still observed. This V_O induces Cu^{2+} and Ti^{4+} to change their oxidation states to Cu^+ and Ti^{3+} as observed via the XPS measurements (Fig. 7). As a result, a small conductive component (semiconducting grains) might be generated by short-range migration of charge due to electrons hopping between $Cu^+ \leftrightarrow Cu^{2+}$ and $Ti^{3+} \leftrightarrow Ti^{4+}$. Therefore, the R_{gb} is larger than R_g . For CCTO ceramic, the differences of resistances between the grain and grain boundary are more than three orders of magnitude. According to Adams *et al.*,⁴⁴ they tested the influences of sintering time to the electrical properties of grain and grain boundary of CCTO ceramic using impedance spectroscopy. At the sintering temperature of 1115 °C, the grain sizes of CCTO ceramics sintered for 3 and 24 h were ~3–5 and ~50–300 μm, respectively. Although the grain size of CCTO ceramic increases, its grain resistance is almost unchanged (R_g of CCTO ceramics sintered for 3 and 24 h were 50 and 30 Ω). Also, the grain boundary resistances (R_{gb}) of this ceramic at these conditions were 4.2 and 0.18 MΩ. This implied that the grain size of CCTO ceramic increases but the R_{gb} is always larger than R_g . Based on our experiments, it was found that our results are consistent with Adams *et al.*'s work. The Z^* spectra indicate an IBLC structure [inset (2) of Fig. 7] in sintered samples. Interestingly, co-doping with Mg^{2+} and Al^{3+} can increase R_g and R_{gb} over that of the CCTO ceramic. According to computational results, it is reasonable to suggest that the increased R_g of the Mg05Al05 ceramic might have originated from suppression of oxygen loss during the sintering process due to dopant influences.

As shown in Structure III of Fig. 6, no V_O was produced at anion positions close to the Al and Mg ions. Also, Mg and Al ions occupied sites independently of other Mg/Al ions, as shown in Structure B of Fig. 5. Therefore, R_g of the Mg05Al05 ceramic can be increased in this way. Interestingly, the origins of the enhanced R_{gb} of this ceramic might have more than one cause. The first cause is similar to an increase in R_g as the V_O concentration in the lattice decreases. Another crucial cause might be the presence of a metastable insulating layer produced by the LPS mechanism. These two factors may result in an enhanced R_{gb} . This result is similar to our earlier findings.^{10–12}

The dielectric properties of CCTO and Mg05Al05 ceramics were systematically examined. Frequency dependencies of ϵ' and $\tan \delta$ at 30 °C are shown in Fig. 8 and its inset (1). The ϵ' values of the Mg05Al05 ceramic are much larger than those of the CCTO ceramic throughout a frequency range of 40 to 10^4 Hz. Additionally, the ϵ' value of the co-doped ceramic has much more frequency stability than that of the pure sample over this frequency range. As listed in Table 2, ϵ' at 1 kHz of CCTO and Mg05Al05 ceramics were 23 062 and 58 397, respectively. The difference of ϵ' values between these two samples is consistent with their microstructural factors.

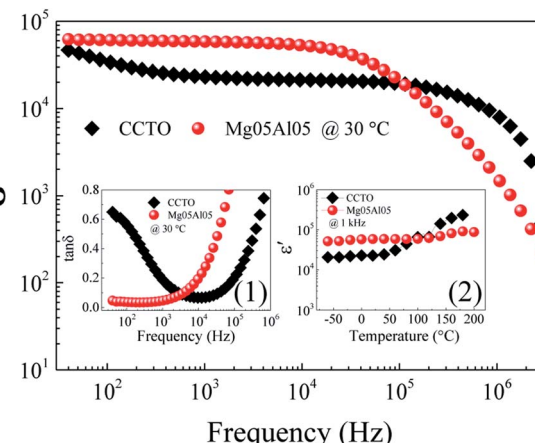


Fig. 8 Frequency dependencies at 30 °C of ϵ' of CCTO and Mg05Al05 ceramics. Insets (1) and (2) show the frequency dependency of $\tan \delta$ and the temperature dependency of ϵ' at 1 kHz, respectively.

Interestingly, although the number of GB layers per unit volume of Mg05Al05 ceramic decreases, the total R_{gb} of Mg05Al05 ceramic is much larger than that of the pure CCTO ceramic. However, a substantial contribution of a sample–electrode contact was found in the CCTO sample due to its low resistance (its Z^* spectra at 110 °C is given in the ESI†). In general, the influence of a sample–electrode contact has usually occurred in the low resistive materials or a specific environment that induces the material's resistance to decrease, for example, under DC bias.⁹

With removal of the impact of a sample–electrode contact from R_{gb} calculation, a complex electric modulus ($M^* = M' + jM''$) can be considered. A M^* plot can be calculated using the following equations:

$$M^* = j\omega C_0 Z^* = M' + jM'' \quad (2)$$

$$M''_{\max} = C_0 / 2C_{gb} \quad (3)$$

$$\omega \tau_{gb} = \omega R_{gb} C_{gb} = 1 \quad (4)$$

M''_{\max} is the maximal value of M'' , $\tau_{gb} = 1/\omega_{\max}$ is the variation of relaxation time. The R_{gb} at 110 °C estimated from M^* plots of CCTO and Mg05Al05 ceramics were 2.04×10^3 and 1.33×10^5 Ω cm, respectively. Enhanced R_{gb} in Mg05Al05 ceramic results in a reduction of its low-frequency $\tan \delta$ compared to that of CCTO, as shown in inset (2) of Fig. 8. The $\tan \delta$ values at 1 kHz of CCTO and Mg05Al05 ceramics were 0.185 and 0.047, respectively. In addition to enhancing ϵ' and reducing $\tan \delta$, co-

Table 2 ϵ' and $\tan \delta$ at 1 kHz and 30 °C, R_g at 30 °C, R_{gb} at 110 °C, activation energies of GBs (E_{gb}) of the CCTO and Mg05Al05 ceramics

| Sample | ϵ' | $\tan \delta$ | R_g (Ω cm) | R_{gb} (Ω cm) | E_g (eV) | E_{gb} (eV) |
|----------|-------------|---------------|--------------|--------------------|------------|---------------|
| CCTO | 23 062 | 0.185 | 155 | 2.04×10^3 | 0.077 | 0.599 |
| Mg05Al05 | 58 397 | 0.047 | 430 | 1.33×10^5 | 0.116 | 0.796 |



doping with Mg^{2+} and Al^{3+} can suppress variations of ϵ' at 1 kHz throughout a temperature range of -60 to 130 $^{\circ}C$, as shown in inset (2) of Fig. 8. Compared to $Ca_{0.95}Sr_{0.05}Cu_3Ti_{3.95}Ge_{0.05}O_{12}$ ceramic,¹² the dielectric permittivity and loss tangent of the Mg05Al05 are still acceptable for capacitor applications, namely dielectric permittivity ≥ 5000 and loss tangent ≤ 0.05 at 1000 ± 50 Hz at room temperature. Also, the temperature stability of the dielectric permittivity in the Mg05Al05 sample is higher than that in the $Ca_{0.95}Sr_{0.05}Cu_3Ti_{3.95}Ge_{0.05}O_{12}$ ceramic. For Mg05Al05 samples, the temperature coefficient of dielectric permittivity at 1000 ± 50 Hz ($\Delta\epsilon'/\epsilon'_{30\text{ }^{\circ}C}$) is rather stable over the temperature range of -60 to 130 $^{\circ}C$, whereas, this coefficient is unchanged in the temperature range of -60 to 100 $^{\circ}C$ for $Ca_{0.95}Sr_{0.05}Cu_3Ti_{3.95}Ge_{0.05}O_{12}$. As previously mentioned, the dielectric property of the $Ca_{0.95}Sr_{0.05}Cu_3Ti_{3.95}Ge_{0.05}O_{12}$ ceramic (ref. 12) satisfies the X5R capacitor. Interestingly, the temperature stability of dielectric permittivity of the Mg05Al05 sample meets the standard of the X7R capacitor, which is better than X5R capacitor.

Frequency dependencies of M' and M'' of sintered samples are shown in Fig. 9. The trends for the change in the M''_{max} position for both CCTO and Mg05Al05 ceramics were similar. As soon as the temperature increased, the M''_{max} position immediately moved to a higher frequency, showing thermal dielectric relaxation.²⁸ Furthermore, this behaviour also specified a decrease of R_{gb} with a temperature increase. In the case of R_g , this electrical factor can be reduced by increasing temperature [data not shown].

For grains (E_g) and GBs (E_{gb}), the activation energies were evaluated by using the Arrhenius law, as follows:

$$R_{\text{g,gb}} = R_0 \exp\left(\frac{E_{\text{g,gb}}}{k_B T}\right) \quad (5)$$

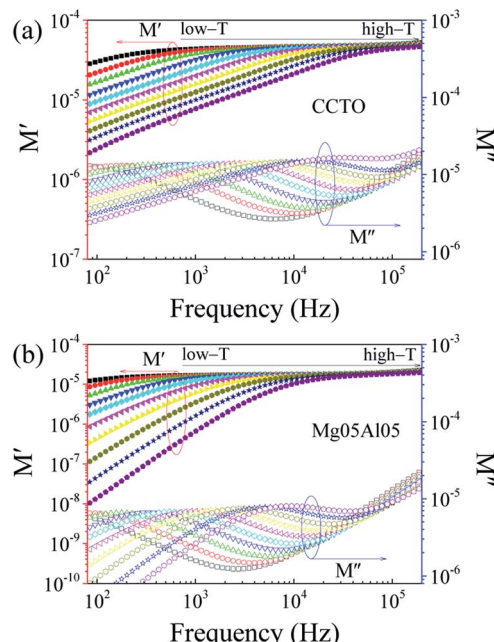


Fig. 9 Frequency dependencies of M' and M'' over a wide temperature range for (a) CCTO and (b) Mg05Al05 ceramics.

where k_B is the Boltzmann constant, and T is the absolute temperature, and R_0 is the pre-exponential constant term. As shown in Fig. 10, the Arrhenius law could fit the temperature dependencies of R_g and R_{gb} well. The E_g and E_{gb} values estimated from slopes of fitting lines are listed in Table 2. Both E_g and E_{gb} of the Mg05Al05 ceramic are greater than that of the CCTO sample, especially the E_{gb} value. The E_g values of CCTO and Mg05Al05 ceramics were 0.077 and 0.116 eV ($\Delta E_g \approx 0.039$ eV). In inset (1) of Fig. 7, the R_g values of CCTO and Mg05Al05 ceramics are consistent with their E_g . The estimated R_g values of CCTO and Mg05Al05 were 155 and 430 Ω cm, respectively. A slight increase in E_g is consistent with the decreased V_O density in the co-doped sample. Remarkably, the difference between E_{gb} (ΔE_{gb}) of CCTO and Mg05Al05 is ≈ 0.197 eV. The E_g of CCTO and Mg05Al05 ceramics were 0.599 and 0.796 eV, respectively. Enhanced R_{gb} and E_{gb} values observed in the co-doped ceramic are closely consistent with their decreased low-frequency $\tan \delta$ values. Oxygen enrichment and the metastable insulating layer at GBs might substantially impact the enhanced dielectric response, especially the reduced $\tan \delta$ value.

The XPS spectra of Cu and Ti ions are illustrated in Fig. 11, showing the oxidations states of these two elements. The XPS spectra of Cu2p and Ti2p were measured in the binding energy (BE) ranges of ~ 926 –970 and 448–470 eV, respectively. The XPS data of transition metal ions were fitted using MultiPak software based on Gaussian–Lorentzian profile fitting. As shown in Fig. 11(a and b), the XPS Cu2p_{3/2} peaks of the CCTO and Mg05Al05 ceramics showed the mixing of Cu⁺ and Cu²⁺ ions. The prominent peak indicating Cu²⁺ was found at a BE value of ~ 933.89 –934.18 eV. The minor peak observed at BE ~ 932.80 –933.20 eV indicates the presence of Cu⁺. The ratios of Cu⁺/Cu²⁺ in CCTO and Mg05Al05 ceramics were $\sim 20.70/79.30\%$ and $\sim 14.02/85.98\%$, respectively.

The oxidation states of Ti were also examined. Both Ti³⁺ and Ti⁴⁺ were found in XPS Ti2p_{3/2} and Ti2p_{1/2} peaks, as shown in Fig. 11(c and d). In the Ti2p_{3/2} peak, the primary peak position indicates that the Ti⁴⁺ state could be found at a BE value of ~ 458.09 –458.21 eV. Simultaneously, a minimal peak of Ti³⁺ was detected at ~ 457.11 –457.20 eV. The ratios of Ti³⁺/Ti⁴⁺ in CCTO and Mg05Al05 ceramics were $\sim 4.20/95.80$ and $\sim 2.75/97.25\%$,

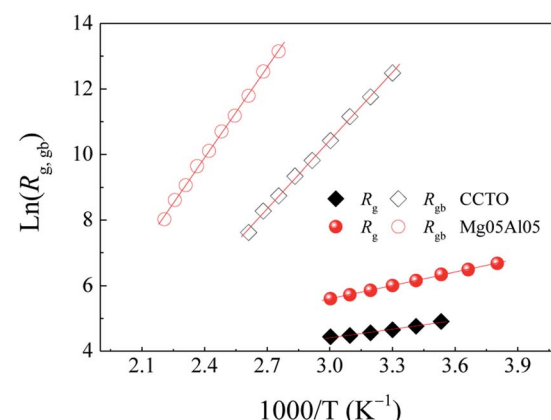


Fig. 10 Arrhenius plots of R_g (solid symbols) and the estimated R_{gb} (open symbols) of CCTO and Mg05Al05 ceramics.



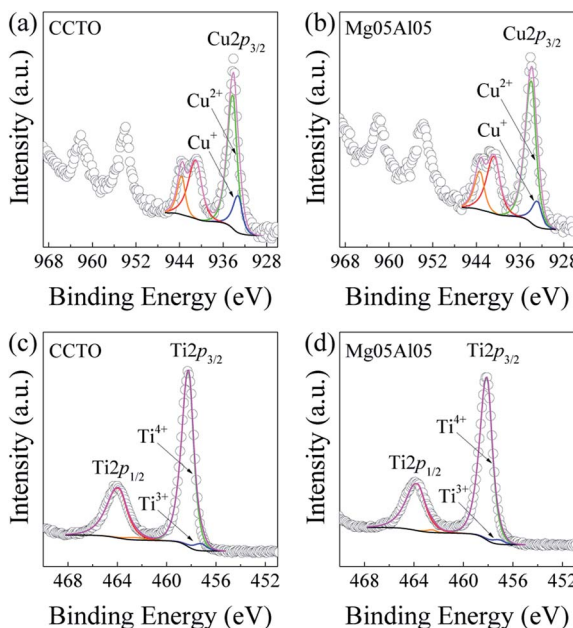


Fig. 11 (a and b) XPS Cu2p spectra of CCTO and Mg05Al05 ceramics, respectively. (c and d) XPS Ti2p spectra of these respective ceramics.

respectively. The existence of Cu^+ and Ti^{3+} signifies the existence of V_O 's in the ceramic lattice, inducing the structure's charge compensation mechanism to obtain a charge balance. Interestingly, percentages of Cu^+ and Ti^{3+} are closely related to the R_g value of each sample. Besides investigating the Cu2p and Ti2p spectra, the O1s spectra were also inspected (data have been included in the ESI†). The examination shows that the O1s spectra were separated to obtain two peaks. The first peak was detected at the BE position ~ 529.63 – 529.70 eV and the second peak can be observed at BE position ~ 531.41 – 531.46 eV. The first oxygen peak depicts oxygen bonded in the lattice (O_L), while the second oxygen peak indicates oxygen-deficient, showing the presence of unbounded oxygen molecules or V_O .⁴⁵ The ratios between $\text{O}_\text{L}/\text{V}_\text{O}$ of the CCTO and Mg05Al05 ceramics were 59.81/40.19 and 67.51/32.49%, respectively. Interestingly, the XPS specifies that the substitutions of Mg^{2+} and Al^{3+} into the CCTO lattice could suppress oxygen loss during the sintering process at relatively high temperatures (V_O decreased), which is consistent with the computational results. According to the previous work, the charge carrier hopping between $\text{Cu}^+ \leftrightarrow \text{Cu}^{2+}$ and $\text{Ti}^{3+} \leftrightarrow \text{Ti}^{4+}$ induces a small conductivity inside the grains;^{28,46} therefore, a slight increase in R_g of the Mg05Al05 ceramic might be caused by a decrease of Cu^+ and Ti^{3+} (V_O decreases). Also, the n-type semiconductive region inside the grains might have been from charge carrier hopping between $\text{Cu}^+ \leftrightarrow \text{Cu}^{2+}$ and $\text{Ti}^{3+} \leftrightarrow \text{Ti}^{4+}$. Therefore, the origin of colossal dielectric permittivity might have been derived from an IBLC effect.

Conclusions

This work deals with the dielectric, electrical, and structural properties of (Mg, Al) co-doped $\text{CaCu}_3\text{Ti}_4\text{O}_{12}$. The XRD data of

all sintered ceramics show a single phase of $\text{CaCu}_3\text{Ti}_4\text{O}_{12}$. DFT results confirm that Mg^{2+} and Al^{3+} dopant ions occupied Cu^{2+} sites. These results are consistent with the very great grain size expansion due to the liquid-phase sintering mechanism. The enhancement of dielectric properties with very high dielectric permittivity of about 58 397 and a low loss tangent of about 0.047 was accomplished in a $\text{CaCu}_{2.95}\text{Mg}_{0.05}\text{Ti}_{3.95}\text{Al}_{0.05}\text{O}_{12}$ ceramic. Additionally, the temperature stability of the dielectric response was improved. The results of this work indicate that the colossal dielectric properties of these samples are associated with an internal barrier layer capacitor model. The XPS results show the presence of Cu^+ and Ti^{3+} , which might be one of many vital contributing factors to n-type semiconducting grains in $\text{CaCu}_3\text{Ti}_4\text{O}_{12}$ based ceramics.

Author contributions

J. B., P. T., and P. S. designed this project. J. B. and P. S. performed experiments and computations. J. B., J. M., S. K., P. T., and P. S. analysed the computational and experimental data. J. B. and P. S. write the manuscript.

Conflicts of interest

The authors declare no competing financial interests.

Acknowledgements

We would like to acknowledge the Basic Research Fund of Khon Kaen University for financial funding. This project has been supported by Research and Graduate Studies, Khon Kaen University. Also, this work has been partially supported by the Research Network NANOTEC (RNN) program of the National Nanotechnology Center (NANOTEC), NSTDA, Ministry of Higher Education, Science, Research and Innovation (MHESI), and Khon Kaen University, Thailand (Grant No. P1851882).

References

- Y. Yu, J. Yang, J. Wu, X. Gao, L. Bian, X. Li, X. Xin, Z. Yu, W. Chen and S. Dong, *J. Eur. Ceram. Soc.*, 2020, **40**, 3003–3010.
- H. M. Kotb, M. M. Ahmad, S. Aldabal, A. Alshoaibi and A. Aljaafari, *J. Mater. Sci.: Mater. Electron.*, 2019, **30**, 18259–18267.
- J. Sun, C. Xu, X. Zhao, J. Liang and R. Liao, *IEEE Trans. Dielectr. Electr. Insul.*, 2020, **27**, 1400–1408.
- C. Xu, X. Zhao, L. Ren, J. Sun, L. Yang, J. Guo and R. Liao, *J. Alloys Compd.*, 2019, **792**, 1079–1087.
- D. Xu, X. Yue, J. Song, S. Zhong, J. Ma, L. Bao, L. Zhang and S. Du, *Ceram. Int.*, 2019, **45**, 11421–11427.
- J. Tang, Y. Teng, Y. Chen, X. Zhao, S. Wang, W. Wang and R. Ahuja, *Ceram. Int.*, 2021, **47**, 10006–10012.
- W. Wan, W. Tang, M. Tao, H. Cao, J. Luo, W.-x. Yuan and T. Qiu, *J. Mater. Sci.: Mater. Electron.*, 2020, **31**, 5360–5367.
- P. Mao, J. Wang, S. Liu, L. Zhang, Y. Zhao and L. He, *J. Alloys Compd.*, 2019, **778**, 625–632.



9 K. Wu, Y. Huang, L. Hou, Z. Tang, J. Li and S. Li, *J. Mater. Sci.: Mater. Electron.*, 2018, **29**, 4488–4494.

10 J. Boonlakhorn, P. Kidkhunthod and P. Thongbai, *Mater. Today Commun.*, 2019, **21**, 100633.

11 J. Boonlakhorn, J. Prachamon, J. Manyam, P. Thongbai and P. Srepusharawoot, *Ceram. Int.*, 2021, **47**, 13415–13422.

12 J. Boonlakhorn, N. Chanlek, P. Thongbai and P. Srepusharawoot, *J. Phys. Chem. C*, 2020, **124**, 20682–20692.

13 W. Hu, K. Lau, Y. Liu, R. L. Withers, H. Chen, L. Fu, B. Gong and W. Hutchison, *Chem. Mater.*, 2015, **27**, 4934–4942.

14 W. Hu, Y. Liu, R. L. Withers, T. J. Frankcombe, L. Norén, A. Snashall, M. Kitchin, P. Smith, B. Gong, H. Chen, J. Schieler, F. Brink and J. Wong-Leung, *Nat. Mater.*, 2013, **12**, 821–826.

15 X. Wei, W. Jie, Z. Yang, F. Zheng, H. Zeng, Y. Liu and J. Hao, *J. Mater. Chem. C*, 2015, **3**, 11005–11010.

16 H. Peng, B. Shang, X. Wang, Z. Peng, X. Chao, P. Liang and Z. Yang, *Ceram. Int.*, 2018, **44**, 5768–5773.

17 Z. Cao, J. Zhao, J. Fan, G. Li and H. Zhang, *Ceram. Int.*, 2021, **47**, 6711–6719.

18 M. Maleki Shahraki, M. Golmohammad, M. D. Chermahini, P. Mahmoudi and H. A. Moghadam, *Mater. Chem. Phys.*, 2020, **246**, 122843.

19 Y. Song, X. Wang, X. Zhang, X. Qi, Z. Liu, L. Zhang, Y. Zhang, Y. Wang, Y. Sui and B. Song, *Appl. Phys. Lett.*, 2016, **109**, 142903.

20 L. L. Kozlinskei, A. T. de Andrade Paes, E. C. Grzebielucka, C. P. F. Borges, A. V. C. de Andrade, E. C. F. de Souza and S. R. M. Antunes, *Appl. Phys. A*, 2020, **126**, 447.

21 P. Kum-onsa, N. Phromviyo and P. Thongbai, *RSC Adv.*, 2020, **10**, 40442–40449.

22 P. Kum-onsa, N. Phromviyo and P. Thongbai, *Results Phys.*, 2020, **18**, 103312.

23 Y. Yu, X. Wang, X. Wang, X. Li, L. Weng and X. Zhang, *J. Mater. Sci.: Mater. Electron.*, 2020, **31**, 18336–18343.

24 A. Sasmal, A. Patra, P. S. Devi and S. Sen, *Dalton Trans.*, 2021, **50**, 1824–1837.

25 D. C. Sinclair, T. B. Adams, F. D. Morrison and A. R. West, *Appl. Phys. Lett.*, 2002, **80**, 2153.

26 M. S. Ivanov, F. Amaral, V. A. Khomchenko, J. A. Paixão and L. C. Costa, *RSC Adv.*, 2017, **7**, 40695–40704.

27 S. Y. Chung, I. D. Kim and S. J. L. Kang, *Nat. Mater.*, 2004, **3**, 774–778.

28 L. Ni and X. M. Chen, *Solid State Commun.*, 2009, **149**, 379–383.

29 S. Ke, H. Huang and H. Fan, *Appl. Phys. Lett.*, 2006, **89**, 182904.

30 J. Boonlakhorn, J. Prachamon, J. Manyam, S. Krongsuk, P. Thongbai and P. Srepusharawoot, *RSC Adv.*, 2021, **11**, 16396–16403.

31 W. Jian, S.-P. Wang, H.-X. Zhang and F.-Q. Bai, *Inorg. Chem. Front.*, 2019, **6**, 2660–2666.

32 B. Li and H. Metiu, *J. Phys. Chem. C*, 2010, **114**, 12234–12244.

33 H.-Y. Su and K. Sun, *J. Mater. Sci.*, 2015, **50**, 1701–1709.

34 J. Boonlakhorn, P. Thongbai, B. Putasaeng, P. Kidkhunthod, S. Maensiri and P. Chindaprasirt, *J. Am. Ceram. Soc.*, 2017, **100**, 3478–3487.

35 G. Kresse and J. Furthmüller, *Comput. Mater. Sci.*, 1996, **6**, 15–50.

36 M. A. Subramanian, D. Li, N. Duan, B. A. Reisner and A. W. Sleight, *J. Solid State Chem.*, 2000, **151**, 323–325.

37 E. Jansen, W. Schafer and G. Will, *J. Appl. Crystallogr.*, 1994, **27**, 492–496.

38 L. Sun, R. Zhang, Z. Wang, E. Cao, Y. Zhang and L. Ju, *J. Alloys Compd.*, 2016, **663**, 345–350.

39 A. Nautiyal, C. Autret, C. Honstettre, S. De Almeida Didry, M. El Amrani, S. Roger, B. Negulescu and A. Ruyter, *J. Eur. Ceram. Soc.*, 2016, **36**, 1391–1398.

40 S. W. Choi, S. H. Hong and Y. M. Kim, *J. Am. Ceram. Soc.*, 2007, **90**, 4009–4011.

41 R. D. Shannon, *Acta Crystallogr., Sect. A: Cryst. Phys., Diff., Theor. Gen. Crystallogr.*, 1976, **32**, 751–767.

42 G. J. Janz, C. B. Allen, N. P. Bansal, R. M. Murphy and R. P. T. Tomkins, *Physical properties data compilations relevant to energy storage, 1. Molten salts: Eutectic Data*, 1979.

43 S. Y. Lee, H. E. Kim and S. I. Yoo, *J. Am. Ceram. Soc.*, 2014, **97**, 2416–2419.

44 T. B. Adams, D. C. Sinclair and A. R. West, *J. Am. Ceram. Soc.*, 2006, **89**, 3129–3135.

45 T. Kim, G. Baek, S. Yang, J. Y. Yang, K. S. Yoon, S. G. Kim, J. Y. Lee, H. S. Im and J. P. Hong, *Sci. Rep.*, 2018, **8**, 8532.

46 X. J. Luo, Y. T. Zhang, D. H. Xu, S. S. Chen, Y. Wang, Y. Chai, Y. S. Liu, S. L. Tang, C. P. Yang and K. Bärner, *Ceram. Int.*, 2019, **45**, 12994–13003.

